

Realizability-preserving finite element discretizations of the M_1 model for dose calculation in proton therapy

Paul Moujaes^{a,*}, Dmitri Kuzmin^a, Christian Bäumer^{b,c,d,e}

^a*Institute of Applied Mathematics (LS III), TU Dortmund University
Vogelpothsweg 87, 44227 Dortmund, Germany*

^b*West German Proton Therapy Centre Essen (WPE) gGmbH
Am Mühlenbach 1, 45147 Essen, Germany*

^c*West German Cancer Center (WTZ), Hufelandstr. 55, 45147 Essen, University Hospital Essen, Essen, Germany*

^d*German Cancer Consortium (DKTK), Hufelandstr. 55, 45147 Essen, Germany*

^e*Department of Physics, TU Dortmund University, Otto-Hahn-Str. 4, 44227 Dortmund, Germany*

Abstract

We present a deterministic framework for proton therapy dose calculation based on finite element discretizations of the energy-dependent M_1 moment model. The nonlinear M_1 system is derived from the Fokker–Planck equation for charged particles and closed using an entropy-based approximation of the second moment. Energy is treated as a pseudo-time coordinate. The zeroth and first moments of the proton fluence are evolved backward in energy. To ensure hyperbolicity and physical admissibility, we employ a monolithic convex limiting (MCL) strategy. Representing the standard continuous Galerkin discretization in terms of auxiliary ‘bar’ states, we construct a nonlinear scheme that is provably invariant domain preserving (IDP) w.r.t. convex realizable sets consisting of all admissible states. The realizability of the bar states is enforced using the MCL technology for homogeneous hyperbolic systems. The forcing induced by stiff scattering is incorporated using Strang-type operator splitting. We use an explicit strong-stability-preserving Runge–Kutta method for the radiation transport subproblem and exact integration in the forcing steps, which guarantees the IDP property. The deposited dose is defined as the integral of a weighted zeroth moment over a bounded energy range. It is accumulated during the backward-in-energy evolution. Numerical experiments demonstrate that the proposed Strang-MCL method produces accurate and physically consistent dose distributions.

Keywords: proton therapy, radiative transfer, realizable moment models, hyperbolic balance laws, finite elements, invariant domain preservation, flux limiting

*Corresponding author

Email addresses: paul.moujaes@math.tu-dortmund.de (Paul Moujaes), kuzmin@math.uni-dortmund.de (Dmitri Kuzmin), Christian.Baeumer@uk-essen.de (Christian Bäumer)

1. Introduction

Proton therapy enables precise dose delivery to cancerous tissue while minimizing damage to surrounding healthy tissue. This remarkable capability arises from the so-called Bragg peak effect, a highly localized energy deposition occurring near the end of the proton range. Accurate prediction of the Bragg peak and the resulting dose distribution in patients is therefore essential for treatment planning. To date, Monte Carlo algorithms are widely regarded as the standard for clinical dose calculations [28, 37, 51, 56]. Despite their high accuracy, the substantial computational effort required by these methods remains a major challenge for routine clinical use.

Deterministic models, such as the Boltzmann transport equation and its Fokker–Planck approximation for charged particles, offer a promising alternative for dose calculation in radiotherapy [7, 22, 52, 53, 55]. The physical processes governing dose distribution include energy loss due to ionization and the lateral spreading of proton beams caused by multiple Coulomb scattering. These effects are modeled by the stopping power [11, 54] and the scattering power [23], respectively. The proton fluence depends on space, energy, and direction of flight, resulting in a high-dimensional phase space.

Moment models, such as the M_1 model, provide a favorable compromise between accuracy and computational cost [10, 18, 50, 21]. The nonlinear M_1 system evolves the zeroth and first angular moments of the particle fluence. Since the number of unknowns exceeds the number of equations, the system must be closed by an additional relation that expresses the second angular moment in terms of the zeroth and first moments. Such closures can be constructed, e.g., using the maximum entropy principle [1, 12, 13, 16, 21, 20, 26, 36, 35, 41, 42, 49]. Physical consistency requires that the reconstructed moments remain within a convex *realizable set* of angular moments associated with nonnegative probability distributions [9, 29, 48]. Entropy-based closures guarantee this property.

A discontinuous Galerkin (DG) method using slope limiters to ensure realizability for the time-dependent but energy-independent M_1 model can be found in [15]. The limiting strategies considered in [15] were found to introduce nonphysical disturbances. A realizable and nonoscillatory continuous finite element discretization of the same model was designed in our recent work [45] using a combination of the monolithic convex limiting (MCL) framework [30] for hyperbolic systems of conservation laws and Patankar’s method [14] for positivity-preserving inclusion of source terms.

In the present work, we extend the steady-state MCL formulation to account for the energy dependence and the presence of the stopping power in the energy derivative. Treating the energy variable as a pseudo-time coordinate, we employ a backward marching method for energy discretization. Instead of treating the reactive forcing terms due to stiff scattering implicitly as in [45], we decouple them from the homogeneous M_1 system using Strang-type operator splitting. The fractional-step Strang-MCL algorithm guarantees positivity preservation for the zeroth moment and enforces the *realizable velocity* constraint for the first moment. These two moments can be interpreted as density and momentum, respectively. The application of MCL in the hyperbolic transport step and exact integration in the forcing step keep the nodal states in the realizable set of the M_1 model. From a formal mathematical perspective, our fully discrete scheme is provably *invariant domain preserving* (IDP).

The deposited dose is computed by integrating the product of the zeroth moment and the stopping power over a finite energy interval. During the backward-in-energy evolution of the moments, the

contribution of each energy step to the cumulative dose is calculated using the trapezoidal quadrature rule. The energy stepping is terminated at a small cutoff energy, at which point the remaining energy is assumed to be deposited locally. The results of our numerical studies for prototypical proton therapy scenarios are free of spurious oscillations and fully consistent with the underlying physics.

The remainder of this paper is organized as follows. Section 2 introduces the high-dimensional proton transport model, the corresponding M_1 moment approximation, and an entropy-based closure. In Section 3.2, we present a low-order discretization that ensures the IDP property, i.e., realizability. The MCL algorithm that imposes global and local bounds on the quantities of interest in the flux-corrected high-order extension is described in Section 3.3. The procedure for dose calculation is outlined in Section 3.4. Numerical results are reported in Section 4, followed by conclusions in Section 5.

2. Proton transport modeling

We begin with a review of two popular radiative transfer models for applications in proton therapy.

2.1. Fokker-Planck equation

The steady-state continuous slowing down Fokker–Planck approximation of the linear Boltzmann equation reads [7, 21, 22]

$$\boldsymbol{\Omega} \cdot \nabla_{\mathbf{x}} \psi(\mathbf{x}, \boldsymbol{\Omega}, E) - \frac{\partial(S(\mathbf{x}, E)\psi(\mathbf{x}, \boldsymbol{\Omega}, E))}{\partial E} = \frac{T(\mathbf{x}, E)}{2} \Delta_{\boldsymbol{\Omega}} \psi(\mathbf{x}, \boldsymbol{\Omega}, E), \quad (1)$$

where $\psi(\mathbf{x}, \boldsymbol{\Omega}, E) \geq 0$ denotes the proton fluence at position $\mathbf{x} \in \mathcal{D} \subset \mathbb{R}^d$, $d \in \{1, 2, 3\}$, moving in direction $\boldsymbol{\Omega} \in \mathbb{S}^{d-1} = \{\boldsymbol{\Omega}' \in \mathbb{R}^d : |\boldsymbol{\Omega}'| = 1\}$ with energy $E \in [0, E_{\max}]$. The physical meaning and modeling of the scaling functions $S(\mathbf{x}, E)$ and $T(\mathbf{x}, E)$ are explained below. For simplicity, we omit the explicit dependence on \mathbf{x} in the models introduced below.

The stopping power $S(E) := -\frac{dE}{dx}$ represents the mean energy loss per unit path length. There exist published data sets [8] and parameterizations [46] for $S(E)$. In this work, we adopt the Bragg–Kleeman rule [4, 11, 54], which approximates $S(E)$ by

$$S(E) = \frac{1}{\beta p} E^{1-p}. \quad (2)$$

This parametrization is derived from the continuous slowing-down range

$$R(E) = \beta E^p, \quad (3)$$

which represents the range of a monoenergetic proton beam in a homogeneous medium. The parameters $\beta > 0$ and $p \in [1, 2]$ are typically fitted to experimental data and depend on the material [46, 54]. For heterogeneous media, these parameters are commonly chosen to be piecewise constant in space, i.e., constant within each material slab [17]. The Bragg–Kleeman model provides sufficient accuracy while remaining computationally simple compared to other parameterizations [54].

Remark 1. The numerical methods proposed below are compatible with any stopping power, provided it remains physically meaningful, i.e., strictly positive.

The projected scattering power $T(E) > 0$, also known as the angular diffusion coefficient, represents the rate at which a proton beam spreads laterally due to multiple small-angle Coulomb scatterings as it travels through a material. We adopt the Rossi parameterization [23]

$$T(E) = \left(\frac{E_s}{pv}\right)^2 \frac{1}{X_S}, \quad (4)$$

where $E_s = 15.0$ MeV, while p and v are the momentum and velocity of the proton, respectively. The quantity pv , which depends on the proton energy E , is defined as

$$pv = \frac{\tau + 2}{\tau + 1}E, \quad \tau = \frac{E}{mc^2}, \quad (5)$$

where $mc^2 = 938.272$ MeV is the rest energy of protons. The quantity X_S denotes the scattering length [23] and is given by

$$\frac{1}{\rho X_S} = \alpha N_A r_e^2 \frac{Z^2}{A} \left(2 \ln \left(33219(AZ)^{-\frac{1}{3}}\right) - 1\right), \quad (6)$$

where $\alpha \approx \frac{1}{137}$ is the fine-structure constant, $N_A = 6.0221408 \times 10^{23}$ is Avogadro's number, $r_e = 2.81796 \times 10^{-13}$ cm is the classical electron radius, and ρ , A , and Z denote the mass density, atomic weight, and atomic number of the target material, respectively. For compound or mixed materials, the scattering length can be computed using the Bragg rule [23]

$$\frac{1}{\rho X_S} = \sum_m w_m \left(\frac{1}{\rho X_S}\right)_m, \quad (7)$$

where w_m is the fraction by weight of the m -th constituent, which we obtain from [47, Table 5.1]. Similarly to stopping power, the spatial dependence of the scattering power results from the material dependence of these quantities. Table 1 summarizes the model parameters for selected materials.

Material	β	p	X_S	ρ
Water	0.0022	1.77	46.88	1
Muscle	0.0021	1.75	45.88	1.04
Lung	0.0033	1.74	175.58	0.3
Bone	0.0011	1.77	17.93	1.85

Table 1: Bragg–Kleeman parameters [4, Table 1], scattering lengths obtained from (6) and (7), and densities for selected materials.

The main quantity of interest for proton therapy is the dose [27, 34]

$$D(\mathbf{x}) = \frac{1}{\rho(\mathbf{x})} \int_0^{E_{\max}} \int_{\mathbb{S}^{d-1}} S(\mathbf{x}, E) \psi(\mathbf{x}, \boldsymbol{\Omega}, E) d\boldsymbol{\Omega} dE, \quad (8)$$

which is absorbed by the medium.

2.2. M_1 moment model

Numerical solution of the Fokker–Planck equation (1) is computationally expensive due to the high dimensionality of the domain $\mathcal{D} \times \mathbb{S}^{d-1} \times [0, E_{\max}]$. The M_N model approximates (1) by a nonlinear system of equations for the first $N + 1$ angular moments of ψ defined by

$$\psi^{(n)} = \int_{\mathbb{S}^{d-1}} \underbrace{\boldsymbol{\Omega} \otimes \cdots \otimes \boldsymbol{\Omega}}_{n \text{ times}} \psi(\boldsymbol{\Omega}) \, d\boldsymbol{\Omega}, \quad n = 0, \dots, N. \quad (9)$$

The corresponding balance laws are derived by taking angular moments of (1). A suitable closure is required to approximate $\psi^{(N+1)}$ in terms of $\psi^{(0)}, \dots, \psi^{(N)}$. Hereafter, boldface notation is used for angular moments of degree $n > 0$, which represent vector or tensor fields.

Focusing on the case $N = 1$, we consider the M_1 system [18]

$$\nabla \cdot \boldsymbol{\psi}^{(1)} - \frac{\partial (S\psi^{(0)})}{\partial E} = 0, \quad (10)$$

$$\nabla \cdot \boldsymbol{\psi}^{(2)} - \frac{\partial (S\boldsymbol{\psi}^{(1)})}{\partial E} = -T\boldsymbol{\psi}^{(1)}, \quad (11)$$

which consists of coupled equations for the zeroth and first moments

$$\begin{aligned} \psi^{(0)} &= \psi^{(0)}(\mathbf{x}, E) = \int_{\mathbb{S}^{d-1}} \psi(\mathbf{x}, \boldsymbol{\Omega}, E) \, d\boldsymbol{\Omega} \in \mathbb{R}, \\ \boldsymbol{\psi}^{(1)} &= \boldsymbol{\psi}^{(1)}(\mathbf{x}, E) = \int_{\mathbb{S}^{d-1}} \boldsymbol{\Omega} \psi(\mathbf{x}, \boldsymbol{\Omega}, E) \, d\boldsymbol{\Omega} \in \mathbb{R}^d. \end{aligned}$$

The vanishing right-hand side of (10) follows from the self-adjointness of the Laplace–Beltrami operator $\Delta_{\boldsymbol{\Omega}}$ on the unit sphere. Furthermore, each component of the direction vector $\boldsymbol{\Omega} = (O_1, \dots, O_d)$ can be expressed as a linear combination of spherical harmonics of degree $\ell = 1$. These harmonics are eigenfunctions of $\Delta_{\boldsymbol{\Omega}}$ with eigenvalue $\lambda = -\ell(\ell + 1) = -2$. The reactive source term of equation (11) arises from the application of $\Delta_{\boldsymbol{\Omega}}$ to the components of $\boldsymbol{\Omega}$.

The system of angular moment equations (10) and (11) can be cast in the form

$$\nabla \cdot \mathbf{f}(u) - \frac{\partial (Su)}{\partial E} = -\sigma u, \quad (12)$$

where the vector of unknowns u and the matrix $\mathbf{f}(u)$ of corresponding fluxes are given by

$$u = \begin{pmatrix} \psi^{(0)} \\ \boldsymbol{\psi}^{(1)} \end{pmatrix} \in \mathbb{R}^{d+1}, \quad \mathbf{f}(u) = \begin{pmatrix} \boldsymbol{\psi}^{(1)} \\ \boldsymbol{\psi}^{(2)} \end{pmatrix} \in \mathbb{R}^{d \times (d+1)},$$

and $\sigma = \text{diag}(0, T, \dots, T) \in \mathbb{R}^{(d+1) \times (d+1)}$.

Note that the n -th moment is transported via the $(n + 1)$ -st moment. Thus, we require a closure relation for $\boldsymbol{\psi}^{(2)} = \boldsymbol{\psi}^{(2)}(\psi^{(0)}, \boldsymbol{\psi}^{(1)})$ to approximate the second moment

$$\boldsymbol{\psi}^{(2)} = \boldsymbol{\psi}^{(2)}(\mathbf{x}, E) = \int_{\mathbb{S}^{d-1}} \boldsymbol{\Omega} \otimes \boldsymbol{\Omega} \psi(\mathbf{x}, \boldsymbol{\Omega}, E) \, d\boldsymbol{\Omega} \in \mathbb{R}^{d \times d}.$$

To ensure the physical validity of the M_1 model, the closure must guarantee that if $\psi^{(0)}$ and $\boldsymbol{\psi}^{(1)}$ are moments of a nonnegative angular distribution $\psi \geq 0$, the reconstruction $\boldsymbol{\psi}^{(2)}$ corresponds to the second moment of ψ . Such a closure is called realizable in the radiative transfer literature. A common approach for recovering $\boldsymbol{\psi}^{(2)}$ is via (approximate) maximum entropy reconstruction [1, 15, 16, 35, 49]. To avoid solving a potentially ill-conditioned optimization problem at each point $(\mathbf{x}, E) \in \mathcal{D} \times [0, E_{\max}]$, we employ the widely used realizable approximation [35]

$$\boldsymbol{\psi}^{(2)} = \mathbf{D}(\mathbf{v}) \psi^{(0)}, \quad \mathbf{v} = \frac{\boldsymbol{\psi}^{(1)}}{\psi^{(0)}}, \quad (13)$$

where

$$\mathbf{D}(\mathbf{v}) = \frac{1 - \chi(|\mathbf{v}|)}{2} I_d + \frac{3\chi(|\mathbf{v}|) - 1}{2} \frac{\mathbf{v} \otimes \mathbf{v}}{|\mathbf{v}|^2} \quad (14)$$

is the Eddington tensor and

$$\chi(f) = \frac{3 + 4f^2}{5 + 2\sqrt{4 - 3f^2}} \quad (15)$$

is the Eddington factor.

It is easy to verify that the zeroth and first moments of a nonnegative angular function ψ satisfy

$$\psi^{(0)} \geq 0 \quad \text{and} \quad |\boldsymbol{\psi}^{(1)}| \leq \psi^{(0)}, \quad (16)$$

respectively, while $\psi^{(0)} = 0$ if and only if $\psi(\boldsymbol{\Omega}) \equiv 0$. In this trivial case, $|\boldsymbol{\psi}^{(1)}| = \psi^{(0)}$. Equality $|\boldsymbol{\psi}^{(1)}| = \psi^{(0)}$ occurs only for a perfectly collimated beam, corresponding to an angular delta distribution $\psi(\boldsymbol{\Omega}) = \delta(\boldsymbol{\Omega} - \boldsymbol{\Omega}')$ for some $\boldsymbol{\Omega}' \in \mathbb{S}^{d-1}$ [29]. For $|\boldsymbol{\psi}^{(1)}| = \psi^{(0)}$, the directional Jacobian of the flux function, $\mathbf{f}'_{\mathbf{n}}(u) = \frac{\partial}{\partial u}(\mathbf{f}(u) \cdot \mathbf{n})$, becomes non-diagonalizable, and the M_1 system (12) is no longer hyperbolic [15]. Accordingly, we define the *realizable set* of physically admissible states as

$$\mathcal{R}_1 = \left\{ (\psi^{(0)}, \boldsymbol{\psi}^{(1)})^\top \in \mathbb{R}^{d+1} : \psi^{(0)} > 0, |\boldsymbol{\psi}^{(1)}| < \psi^{(0)} \right\}, \quad (17)$$

which corresponds to the set of moments of nonnegative, nontrivial $L^2(\mathbb{S}^{d-1})$ functions. Note that the realizable set is a convex cone. Furthermore, we refer to moments belonging to \mathcal{R}_1 as realizable.

Let $u = (\psi^{(0)}, \boldsymbol{\psi}^{(1)})^\top \in \mathcal{R}_1$ and reconstruct $\boldsymbol{\psi}^{(2)}(u)$ using (13)–(15) with

$$f^2 \leq \chi(f) \leq 1 \quad \text{for } f \in [0, 1].$$

Under these conditions, $\psi^{(0)}$, $\boldsymbol{\psi}^{(1)}$, and $\boldsymbol{\psi}^{(2)}$ represent the zeroth, first, and second moments of a nonnegative angular distribution, respectively [35].

In view of (8), the absorbed dose can be written in terms of the zeroth moment as follows [18]:

$$D(\mathbf{x}) = \frac{1}{\rho(\mathbf{x})} \int_0^{E_{\max}} S(\mathbf{x}, E) \psi^{(0)}(\mathbf{x}, E) dE. \quad (18)$$

3. Discretization and methodology

To construct a realizability-preserving continuous finite element discretization of (12), we first derive a low-order scheme that is invariant-domain preserving (IDP), in the sense that the approximate nodal states remain in the realizable set \mathcal{R}_1 . We then incorporate high-order correction terms and use the monolithic convex limiting (MCL) methodology [30] to enforce the IDP property. For the time-dependent and energy-independent M_1 model, such algorithms were designed in our previous work [45]. In this section, we adapt them to the structure of system (12). The product Su is evolved backward in energy using Strang splitting to decouple the forcing terms arising from scattering. Exact energy integration for the source-term subproblems provides a more accurate IDP treatment than the algorithm employed in [45]. An explicit strongly-stability-preserving Runge–Kutta (SSP-RK) method is used for the homogeneous subsystem of (12). The dose (18) is decomposed into integrals over individual energy evolution steps. These integrals are approximated using the trapezoidal rule.

3.1. High-order method

Let a boundary condition of the form $\mathbf{f}(u) \cdot \mathbf{n} = \mathcal{F}(u, \hat{u}; \mathbf{n})$ be imposed weakly on the boundary $\Gamma = \partial\mathcal{D}$ of the spatial domain $\mathcal{D} \subset \mathbb{R}^3$. Choosing a test function w , we construct the weak form

$$\int_{\mathcal{D}} w \left(\nabla \cdot \mathbf{f}(u) - \frac{\partial(Su)}{\partial E} + \sigma u \right) dx = \int_{\Gamma} w (\mathbf{f}(u) \cdot \mathbf{n} - \mathcal{F}(u, \hat{u}; \mathbf{n})) ds \quad (19)$$

of the M_1 system (12). The boundary term is defined using the global Lax–Friedrichs (GLF) flux

$$\mathcal{F}(u, \hat{u}; \mathbf{n}) = \frac{\mathbf{f}(u) + \mathbf{f}(\hat{u})}{2} \cdot \mathbf{n} - \frac{\lambda_{\max}}{2}(\hat{u} - u),$$

where $\lambda_{\max} = 1$ is a global upper bound for the maximum wave speed [9, 15, 48]. The external state \hat{u} of the boundary condition corresponds to a proton beam.

We discretize the weak form (19) in space using a conforming mesh $\mathcal{T}_h = \{K_e\}_{e=1}^{E_h}$ with cells K_1, \dots, K_{E_h} and vertices $\mathbf{x}_1, \dots, \mathbf{x}_{N_h}$. The Lagrange basis functions of a globally continuous, piecewise linear (\mathbb{P}_1) or multilinear (\mathbb{Q}_1) finite element approximation are denoted by $\varphi_1, \dots, \varphi_{N_h}$. They possess the interpolatory property $\varphi_i(\mathbf{x}_j) = \delta_{ij}$ and span the space $V_h \subset H^1(\mathcal{D}) \cap C(\bar{\mathcal{D}})$.

A *group finite element* approximation (cf. [6, 19]) to the conserved product Su is defined by

$$(Su)_h(\mathbf{x}, E) = \sum_{j=1}^{N_h} (Su)_j(E) \varphi_j(\mathbf{x}). \quad (20)$$

In a similar vein, the nonlinear flux function $\mathbf{f}(u(\mathbf{x}, E))$ of the M_1 model is approximated by

$$\mathbf{f}_h(\mathbf{x}, E) = \sum_{j=1}^{N_h} \mathbf{f}_j(E) \varphi_j(\mathbf{x}), \quad \mathbf{f}_j(E) = \mathbf{f}(u_j(E)). \quad (21)$$

The coefficients $(Su)_j(E) = (Su)_h(\mathbf{x}_j, E)$ of $(Su)_h$ are evolved directly, whereas the nodal states $u_j(E) = u_h(\mathbf{x}_j, E)$ of the corresponding moment approximation

$$u_h(\mathbf{x}, E) = \sum_{j=1}^{N_h} u_j(E) \varphi_j(\mathbf{x}), \quad u_j(E) = \frac{(Su)_j(E)}{S_j(E)}, \quad S_j(E) = S(\mathbf{x}_j, E) \quad (22)$$

are recovered from the main discrete unknowns $(Su)_j(E)$ via division by the nodal stopping power $S_j(E)$. Since the realizable set \mathcal{R}_1 is a convex cone, $(Su)_j \in \mathcal{R}_1$ if and only if $u_j \in \mathcal{R}_1$.

We introduce the index sets $\mathcal{N}_i = \{j \in \{1, \dots, N_h\} : \text{supp}(\varphi_j) \cap \text{supp}(\varphi_i) \neq \emptyset\}$ and $\mathcal{N}_i^* = \mathcal{N}_i \setminus \{i\}$ to define the computational stencils of node i . Using a basis function $w = \varphi_i$ as test function and substituting the finite element approximations (20)–(21) into (19), we obtain

$$-\sum_{j \in \mathcal{N}_i} m_{ij} \frac{d(Su)_j}{dE} = b_i(u_h, \hat{u}) - \sum_{j \in \mathcal{N}_i} [\mathbf{f}_j \cdot \mathbf{c}_{ij} + m_{ij}^\sigma u_j]. \quad (23)$$

The coefficients of this semi-discrete backward-in-energy evolution equation are given by

$$\begin{aligned} m_{ij} &= \int_{\mathcal{D}} \varphi_i \varphi_j \, d\mathbf{x}, \quad \mathbf{c}_{ij} = \int_{\mathcal{D}} \varphi_i \nabla \varphi_j \, d\mathbf{x}, \\ m_{ij}^\sigma &= \text{diag}(0, m_{ij}^T, \dots, m_{ij}^T), \quad m_{ij}^T = \int_{\mathcal{D}} T \varphi_i \varphi_j \, d\mathbf{x}. \end{aligned}$$

The weakly imposed boundary condition is taken into account via

$$b_i(u_h, \hat{u}) = \int_{\Gamma} \varphi_i (\mathbf{f}(u_h) \cdot \mathbf{n} - \mathcal{F}(u_h, \hat{u}; \mathbf{n})) \, ds.$$

Since the standard Galerkin discretization (23) is generally not IDP, we will modify it using a customized version of the MCL procedures developed in [30, 45].

3.2. Low-order method

A fundamental building block of the MCL algorithm to be designed is a low-order scheme that provides provable IDP properties. We derive it from (23) using *mass lumping* (inexact nodal quadrature) and artificial *graph viscosity* of GLF type. The lumped-mass approximations

$$\sum_{j \in \mathcal{N}_i} m_{ij} \frac{d(Su)_j}{dE} \approx m_i \frac{d(Su)_i}{dE}, \quad \sum_{j \in \mathcal{N}_i} m_{ij}^\sigma u_j \approx m_i^\sigma u_i$$

are defined using the row sums of the corresponding consistent mass matrices, i.e.,

$$m_i = \sum_{j \in \mathcal{N}_i} m_{ij} = \int_{\mathcal{D}} \varphi_i \, d\mathbf{x}, \quad m_i^\sigma = \text{diag}(0, m_i^T, \dots, m_i^T), \quad m_i^T = \sum_{j \in \mathcal{N}_i} m_{ij}^T = \int_{\mathcal{D}} T \varphi_i \, d\mathbf{x}.$$

The boundary term $b_i(u_h, \hat{u})$ of problem (23) is approximated by its lumped counterpart

$$\tilde{b}_i(u_i, \hat{u}_i) = \int_{\Gamma} \varphi_i(\mathbf{f}_i \cdot \mathbf{n} - \mathcal{F}(u_i, \hat{u}_i; \mathbf{n})) \, ds. \quad (24)$$

Finally, low-order stabilization via dissipative numerical fluxes of the form $d_{ij}(u_j - u_i)$ is incorporated into the semi-discrete finite element GLF scheme

$$-m_i \frac{d(Su)_i}{dE} = \tilde{b}_i(u_i, \hat{u}_i) + \sum_{j \in \mathcal{N}_i^*} [d_{ij}(u_j - u_i) - (\mathbf{f}_j - \mathbf{f}_i) \cdot \mathbf{c}_{ij}] - m_i^\sigma u_i. \quad (25)$$

The GLF graph viscosity coefficients [33, 45]

$$d_{ij} = \begin{cases} \lambda_{\max} \max\{|\mathbf{c}_{ij}|, |\mathbf{c}_{ji}|\} & \text{if } j \in \mathcal{N}_i^*, \\ -\sum_{k \in \mathcal{N}_i^*} d_{ik} & \text{if } j = i, \\ 0 & \text{otherwise} \end{cases}$$

are defined using the global bound $\lambda_{\max} = 1$ for the realizable maximum speed of the M_1 model.

To show the IDP property of a fully discrete version of (25), we introduce the *bar states* [24, 30, 31]

$$\bar{u}_{ij} = \frac{u_i + u_j}{2} - \frac{(\mathbf{f}_j - \mathbf{f}_i) \cdot \mathbf{c}_{ij}}{2d_{ij}}. \quad (26)$$

As shown in [45], these intermediate states belong to \mathcal{R}_1 if $u_i, u_j \in \mathcal{R}_1$ and $d_{ij} \geq |\mathbf{c}_{ij}|$. For simplicity, we assume i to be an interior node and use (26) to write (25) with $\tilde{b}_i(u_i, \hat{u}_i) = 0$ in the form

$$-m_i \frac{d(Su)_i}{dE} = \sum_{j \in \mathcal{N}_i^*} [2d_{ij}(\bar{u}_{ij} - u_i)] - m_i^\sigma u_i. \quad (27)$$

It is convenient to decompose the bar state form (27) into the following two subproblems:

$$-m_i \frac{d(Su)_i}{dE} = -m_i^\sigma u_i, \quad (28)$$

$$-m_i \frac{d(Su)_i}{dE} = \sum_{j \in \mathcal{N}_i^*} [2d_{ij}(\bar{u}_{ij} - u_i)]. \quad (29)$$

We use this decomposition and the symmetric Strang splitting procedure to advance the numerical solution from the energy level E^{n+1} to $E^n = E^{n+1} - \Delta E$ in three steps [32, Sec. 6.2.7]:

1. Solve the scattering subproblem (28) over a half-step in energy from E^{n+1} to $E^{n+\frac{1}{2}} = E^{n+1} - \frac{\Delta E}{2}$.
2. Starting from the intermediate solution obtained in Step 1, solve the homogeneous radiation transport subproblem (29) over a full step in energy from $E^{n+\frac{1}{2}}$ to E^n .

3. Starting from the intermediate solution obtained in Step 2, solve the scattering subproblem (28) over the second half-step in energy from $E^{n+\frac{1}{2}}$ to the final energy E^n .

We first consider the scattering subproblem (28), which is linear and decouples into independent problems at each node. Let the nodal state

$$(Su)_i^{n+1} = ((S\psi^{(0)})_i^{n+1}, (S\psi^{(1)})_i^{n+1})^\top$$

at energy E^{n+1} be realizable. Since $m_i^\sigma = \text{diag}(0, m_i^T, \dots, m_i^T)$, the equation for the zeroth moment has a vanishing right-hand side, and thus $(S\psi^{(0)})_i^{n+1/2} = (S\psi^{(0)})_i^{n+1}$. The evolution equation

$$-m_i \frac{d(S\psi^{(1)})_i}{dE} = -\frac{m_i^T}{S_i} (S\psi^{(1)})_i \quad (30)$$

for the first moment can be integrated exactly over $[E^{n+1/2}, E^{n+1}]$ and rearranged to obtain

$$(S\psi^{(1)})_i^{n+1/2} = \exp\left(-\frac{1}{m_i} \int_{E^{n+1/2}}^{E^{n+1}} \frac{m_i^T}{S_i} dE\right) (S\psi^{(1)})_i^{n+1}. \quad (31)$$

In practice, the energy integral is approximated using the midpoint rule. This scattering update preserves realizability because $(S\psi^{(0)})_i^{n+1/2} = (S\psi^{(0)})_i^{n+1} > 0$ and

$$\left| (S\psi^{(1)})_i^{n+1/2} \right| \leq \left| (S\psi^{(1)})_i^{n+1} \right| < (S\psi^{(0)})_i^{n+1} = (S\psi^{(0)})_i^{n+1/2}.$$

Next, we consider the transport subproblem (29) on the energy interval from E^{n+1} to E^n starting from the intermediate solution $(Su)_i^{n+1/2} \in \mathcal{R}_1$ obtained with (31). We discretize (29) using an explicit SSP-RK method backwards. Each backward Euler stage can be written as

$$\begin{aligned} (Su)_i^{\text{SSP}} &= (Su)_i + \frac{\Delta E}{m_i} \sum_{j \in \mathcal{N}_i^*} [2d_{ij}(\bar{u}_{ij} - u_i)] \\ &= S_i \left[\left(1 - \frac{\Delta E}{m_i S_i} \sum_{j \in \mathcal{N}_i^*} 2d_{ij} \right) u_i + \frac{\Delta E}{m_i S_i} \sum_{j \in \mathcal{N}_i^*} 2d_{ij} \bar{u}_{ij} \right], \end{aligned} \quad (32)$$

where $(Su)_i$ is defined at E^{n+1} and $(Su)_i^{\text{SSP}}$ at E^n . Under the CFL-like condition

$$\frac{2\Delta E}{m_i S_i} \sum_{j \in \mathcal{N}_i^*} d_{ij} \leq 1, \quad (33)$$

the result $(Su)_i^{\text{SSP}}$ of the explicit update (32) is realizable, because it represents a scaled convex combination of the realizable states u_i and \bar{u}_{ij} , $j \in \mathcal{N}_i^*$.

Remark 2. Similarly to the right-hand side of (29), a nonvanishing boundary term (24) can be written in an IDP bar state form [25, 31, 44]. The realizable external states $u_j = \hat{u}_i$ with indices $j > N_h$ represent the Riemann data of the weakly imposed boundary condition. The corresponding generalization of (29) preserves the realizability of nodal moment states under a suitable restriction on ΔE .

Since the solvers for individual subproblems of the low-order method using Strang splitting are IDP, realizability is also guaranteed for the final solution at the energy level E^n .

3.3. Monolithic convex limiting

The high-order spatial semi-discretization (23) can be recovered from the low-order method (25) by adding antidiffusive fluxes f_{ij} that correct the mass lumping error and offset the diffusive fluxes $d_{ij}(u_j - u_i)$. Let $d_E(Su)_i = \frac{d(Su)_i}{dE}$ denote the nodal energy derivatives corresponding to (23). Then

$$f_{ij} = -m_{ij} \left(d_E(Su)_i - d_E(Su)_j \right) + (d_{ij} + m_{ij}^\sigma)(u_i - u_j). \quad (34)$$

To avoid solving a linear system with the consistent mass matrix $(m_{ij})_{i,j=1}^{N_h}$ and to incorporate high-order stabilization into f_{ij} , we approximate $d_E(Su)_i$ by (cf. [30, 31, 39])

$$d_E(Su)_i^L = \frac{1}{m_i} \left(m_i^\sigma u_i - \sum_{j \in \mathcal{N}_i^*} [d_{ij}(u_j - u_i) - (\mathbf{f}_j - \mathbf{f}_i) \cdot \mathbf{c}_{ij}] \right).$$

Substituting the antidiffusive fluxes (34) into (25) recovers the stabilized high-order target scheme

$$\begin{aligned} -m_i \frac{d(Su)_i}{dE} &= \sum_{j \in \mathcal{N}_i^*} [d_{ij}(u_j - u_i) - (\mathbf{f}_j - \mathbf{f}_i) \cdot \mathbf{c}_{ij} + f_{ij}] - m_i^\sigma u_i \\ &= \sum_{j \in \mathcal{N}_i^*} [2d_{ij}(\bar{u}_{ij}^H - u_i)] - m_i^\sigma u_i. \end{aligned} \quad (35)$$

The high-order bar states

$$\bar{u}_{ij}^H = \bar{u}_{ij} + \frac{f_{ij}}{2d_{ij}} \quad (36)$$

generally do not belong to \mathcal{R}_1 . The monolithic convex limiting (MCL) strategy proposed in [30] replaces the raw antidiffusive fluxes $f_{ij} = -f_{ji}$ by their limited counterparts $f_{ij}^* = -f_{ji}^*$ such that the realizability of $\bar{u}_{ij}, \bar{u}_{ji} \in \mathcal{R}_1$ is preserved by the flux-corrected bar states

$$\bar{u}_{ij}^* = \bar{u}_{ij} + \frac{f_{ij}^*}{2d_{ij}}, \quad \bar{u}_{ji}^* = \bar{u}_{ji} - \frac{f_{ij}^*}{2d_{ij}}. \quad (37)$$

In the MCL version, the radiation transport subproblem of the Strang splitting method is discretized using (29) with \bar{u}_{ij} replaced by \bar{u}_{ij}^* . Since the structure of the low-order scheme is preserved, the backward Euler stages of the explicit SSP-RK method are IDP under the CFL-like condition (33).

In addition to enforcing the physical admissibility conditions $\bar{u}_{ij}^*, \bar{u}_{ji}^* \in \mathcal{R}_1$, a well designed flux limiter should effectively suppress spurious oscillations in the neighborhood of shocks and steep gradients. The MCL procedure employed in [44] achieves numerical admissibility by imposing local discrete maximum principles on the scalar-valued components of the bar states (37).

Let ϕ_i be a component of $u_i = (\psi_i^{(0)}, \psi_{i,1}^{(1)}, \dots, \psi_{i,d}^{(1)})^\top \in \mathcal{R}_1$. The corresponding low-order bar states and raw antidiffusive fluxes are denoted by $\bar{\phi}_{ij}$ and f_{ij}^ϕ , $j \in \mathcal{N}_i^*$, respectively. We formulate the numerical admissibility conditions

$$\begin{aligned} \phi_i^{\min} &\leq \bar{\phi}_{ij}^* = \bar{\phi}_{ij} + \frac{f_{ij}^{\phi,*}}{2d_{ij}} \leq \phi_i^{\max}, \\ \phi_j^{\min} &\leq \bar{\phi}_{ji}^* = \bar{\phi}_{ji} - \frac{f_{ij}^{\phi,*}}{2d_{ij}} \leq \phi_j^{\max} \end{aligned} \quad (38)$$

for the limited antidiffusive fluxes $f_{ij}^{\phi,*}$ using the local bounds

$$\phi_i^{\max} = \max \left\{ \max_{j \in \mathcal{N}_i} \phi_j, \max_{j \in \mathcal{N}_i^*} \bar{\phi}_{ij} \right\}, \quad \phi_i^{\min} = \min \left\{ \min_{j \in \mathcal{N}_i} \phi_j, \min_{j \in \mathcal{N}_i^*} \bar{\phi}_{ij} \right\}. \quad (39)$$

The inequality constraints (38) can be rearranged to

$$\begin{aligned} 2d_{ij} (\phi_i^{\min} - \bar{\phi}_{ij}) &\leq f_{ij}^{\phi,*} \leq 2d_{ij} (\phi_i^{\max} - \bar{\phi}_{ij}), \\ 2d_{ij} (\phi_j^{\min} - \bar{\phi}_{ji}) &\leq -f_{ij}^{\phi,*} \leq 2d_{ij} (\phi_j^{\max} - \bar{\phi}_{ji}). \end{aligned} \quad (40)$$

Introducing the *bounding fluxes*

$$f_{ij}^{\phi,\min} = -f_{ji}^{\phi,\max} = 2d_{ij} \max \{ \phi_i^{\min} - \bar{\phi}_{ij}, \bar{\phi}_{ji} - \phi_j^{\max} \} \leq 0, \quad (41)$$

$$f_{ij}^{\phi,\max} = -f_{ji}^{\phi,\min} = 2d_{ij} \min \{ \phi_i^{\max} - \bar{\phi}_{ij}, \bar{\phi}_{ji} - \phi_j^{\min} \} \geq 0, \quad (42)$$

we set

$$f_{ij}^{\phi,*} = \max \{ f_{ij}^{\phi,\min}, \min \{ f_{ij}^{\phi,\max}, f_{ij}^\phi \} \}. \quad (43)$$

This adjustment of f_{ij}^ϕ ensures the discrete conservation property $f_{ij}^{\phi,*} = -f_{ji}^{\phi,*}$ and the validity of (38) for the bar states. The positivity of the zeroth moment is guaranteed too, since $\bar{\psi}_{ij}^{(0),*} \geq \psi_i^{(0),\min} > 0$ by construction of the local bounds (39). However, enforcing the realizable velocity constraints

$$\left| \bar{\psi}_{ij}^{(1),*} \right| \leq \bar{\psi}_{ij}^{(0),*}, \quad \left| \bar{\psi}_{ji}^{(1),*} \right| \leq \bar{\psi}_{ji}^{(0),*}$$

requires an additional flux limiting step, which was originally proposed in [45] and inspired by a positivity fix for the specific internal energy of the compressible Euler equations [30, 31].

We denote by $f_{ij}^* = (f_{ij}^{*(0)}, \mathbf{f}_{ij}^{*(1)})^\top$ the limited antidiffusive fluxes whose individual components are given by (43). To ensure that the maximum speed corresponding to the final bar state

$$\bar{u}_{ij}^{\text{IDP}} = \bar{u}_{ij} + \frac{\alpha_{ij}^{\text{IDP}} f_{ij}^*}{2d_{ij}} \quad (44)$$

remains bounded by $\lambda_{\max} = 1$, we apply a correction factor $\alpha_{ij}^{\text{IDP}} \in [0, 1]$ such that $\alpha_{ij} = \alpha_{ji}$ and $\bar{u}_{ij}^{\text{IDP}}, \bar{u}_{ji}^{\text{IDP}} \in \mathcal{R}_1$. Written in terms of moments, the IDO constraint for $\bar{u}_{ij}^{\text{IDP}}$ becomes

$$\left| \bar{\psi}_{ij}^{(1)} + \frac{\alpha_{ij}^{\text{IDP}} \mathbf{f}_{ij}^{*(1)}}{2d_{ij}} \right|^2 < \left(\bar{\psi}_{ij}^{(0)} + \frac{\alpha_{ij}^{\text{IDP}} f_{ij}^{*(0)}}{2d_{ij}} \right)^2.$$

This is a quadratic inequality constraint of the form

$$P_{ij}(\alpha_{ij}^{\text{IDP}}) < Q_{ij}, \quad (45)$$

where

$$\begin{aligned} P_{ij}(\alpha) &= \left(\left| \mathbf{f}_{ij}^{*(1)} \right|^2 - \left(f_{ij}^{*(0)} \right)^2 \right) \alpha^2 + 4d_{ij} \left(\bar{\psi}_{ij}^{(1)} \cdot \mathbf{f}_{ij}^{*(1)} - \bar{\psi}_{ij}^{(0)} f_{ij}^{*(0)} \right) \alpha, \\ Q_{ij} &= (2d_{ij})^2 \left(\left(\bar{\psi}_{ij}^{(0)} \right)^2 - \left| \bar{\psi}_{ij}^{(1)} \right|^2 \right) > 0. \end{aligned}$$

For any $\alpha \in [0, 1]$, the estimate $\alpha^2 \leq \alpha$ implies $P_{ij} \leq \alpha R_{ij}$, where

$$R_{ij} = \max \left\{ 0, \left| \mathbf{f}_{ij}^{*(1)} \right|^2 - \left(f_{ij}^{*(0)} \right)^2 \right\} + 4d_{ij} \left(\bar{\psi}_{ij}^{(1)} \cdot \mathbf{f}_{ij}^{*(1)} - \bar{\psi}_{ij}^{(0)} f_{ij}^{*(0)} \right).$$

To enforce the strict inequality (45), we replace \tilde{Q}_{ij} by $\tilde{Q}_{ij} = (1 - \varepsilon)Q_{ij} > 0$ with $\varepsilon = 10^{-15}$. The IDP correction factor

$$\alpha_{ij}^{\text{IDP}} = \begin{cases} \min \left\{ \frac{\tilde{Q}_{ij}}{R_{ij}}, \frac{\tilde{Q}_{ji}}{R_{ji}} \right\} & \text{if } R_{ij} > \tilde{Q}_{ij}, R_{ji} > \tilde{Q}_{ji}, \\ \frac{\tilde{Q}_{ij}}{R_{ij}} & \text{if } R_{ij} > \tilde{Q}_{ij}, R_{ji} \leq \tilde{Q}_{ji}, \\ \frac{\tilde{Q}_{ji}}{R_{ji}} & \text{if } R_{ij} \leq \tilde{Q}_{ij}, R_{ji} > \tilde{Q}_{ji}. \\ 1 & \text{otherwise} \end{cases}$$

satisfies $\alpha_{ij}^{\text{IDP}} = \alpha_{ji}^{\text{IDP}}$. Furthermore, the physical admissibility conditions

$$P_{ij}(\alpha_{ij}^{\text{IDP}}) \leq \alpha_{ij}^{\text{IDP}} R_{ij} \leq \tilde{Q}_{ij} < Q_{ij}, \quad P_{ji}(\alpha_{ij}^{\text{IDP}}) \leq \alpha_{ij}^{\text{IDP}} R_{ji} \leq \tilde{Q}_{ji} < Q_{ji}$$

hold for the final bar states (44). Hence, substituting $\bar{u}_{ij}^{\text{IDP}}$ for \bar{u}_{ij} in (29) yields a numerically admissible and realizability preserving high-order extension

$$\begin{aligned} -m_i \frac{d(Su)_i}{dE} &= \sum_{j \in \mathcal{N}_i^*} [d_{ij}(u_j - u_i) - (\mathbf{f}_j - \mathbf{f}_i) \cdot \mathbf{c}_{ij} + \alpha_{ij}^{\text{IDP}} f_{ij}^*] \\ &= \sum_{j \in \mathcal{N}_i^*} [2d_{ij}(\bar{u}_{ij}^{\text{IDP}} - u_i)] \end{aligned} \quad (46)$$

of the low-order semi-discrete scheme (29) for the transport subproblem of the Strang splitting algorithm. The energy stepping methods remain unchanged for all subproblems.

3.4. Dose calculation

The proposed method treats energy as a pseudo-time variable and advances the numerical solution backward in energy until the threshold $E_{\min} = 10^{-5}$ MeV is reached. The numerical solution and the contributions to the dose are computed at the discrete energy levels

$$E_{\max} = E^N > E^{N-1} > \dots > E^1 = E_{\min}.$$

Stopping at a strictly positive minimum energy E_{\min} avoids the breakdown of physical models, e.g., for the stopping power (2) and the scattering power (4). This ensures that no division by ∞ occurs when computing the integrals in the scattering step (31) or the nodal states $(Su)_i/S_i$ in the transport step. The choice of E_{\max} depends on the boundary conditions.

In a typical numerical experiment for a box domain $\mathcal{D} \subset \mathbb{R}^d$ with inflow boundary

$$\Gamma_{\text{in}} = \{\mathbf{x} = (x_1, \dots, x_d) \in \Gamma : x_1 = 0\},$$

we prescribe the zeroth moment

$$\hat{\psi}^{(0)}(\mathbf{x}, E) = \psi_0 \frac{1}{\sqrt{2\pi} \sigma_E} \exp\left[-\frac{(E - E_0)^2}{2\sigma_E^2}\right] \prod_{k=2}^d \frac{1}{\sqrt{2\pi} \sigma_k} \exp\left[-\frac{(x_k - x_{k,0})^2}{2\sigma_k^2}\right] \quad (47)$$

of a monoenergetic proton beam with energy E_0 . The isocenter of the beam consisting of ψ_0 protons is located at the point $\mathbf{x}_0 = (0, x_{2,0}, \dots, x_{d,0})^\top \in \Gamma_{\text{in}}$. We choose the energy spread $\sigma_E = 0.01 E_0$ and the spatial standard deviation $\sigma_k = 0.3$ for all $k \geq 2$ [52]. In one space dimension, (47) reduces to a Gaussian distribution in energy. The corresponding first moment is prescribed as in [50]

$$\hat{\psi}^{(1)}(\mathbf{x}, E) = f \hat{\psi}^{(0)}(\mathbf{x}, E) \mathbf{e}_1, \quad f = 0.9999, \quad (48)$$

where \mathbf{e}_1 is the unit vector in the x_1 -direction. This choice approximates the moments of a nearly perfectly collimated particle beam. We set $E_{\max} = 1.1 E_0$ to ensure that the full energy spread of the beam is captured.

The initial fluence ψ at E_{\max} is usually assumed to be zero [21]. However, the angular moments associated with the trivial angular distribution lie on the boundary of the realizable set. To avoid this, we prescribe the initial condition [50]

$$\psi^{(0)}(E_{\max}) \equiv 10^{-15}, \quad \psi^{(1)}(E_{\max}) \equiv 0 \quad (49)$$

in the whole domain \mathcal{D} . Multiplying (49) by $S(E_{\max})$, we obtain the initial condition for (Su) .

During the energy stepping, the dose is accumulated using the composite trapezoidal rule, i.e.,

$$\int_{E_{\min}}^{E_{\max}} (S\psi^{(0)})_i \, dE \approx \sum_{n=1}^{N-1} \frac{(S\psi^{(0)})_i^n + (S\psi^{(0)})_i^{n+1}}{2} (E^{n+1} - E^n).$$

The integral over the remaining energy interval $[0, E_{\min}]$ is treated differently. We assume that the proton fluence at energy E_{\min} deposits its residual energy locally. Under this assumption, the stopping power in the interval $[0, E_{\min}]$ is replaced by

$$S_0 = \frac{E_{\min}}{R(E_{\min})}, \quad (50)$$

where $R(E)$ is the proton range given by (3). This treatment is similar to the fictitious group assumption in the context of a multigroup method; see, e.g., [43]. The choice (50) is consistent with the interpretation of the stopping power as the energy loss per unit path length. Thus, we approximate the dose by

$$D(\mathbf{x}) \approx D_h(\mathbf{x}) = \sum_{i=1}^{N_h} D_i \varphi_i(\mathbf{x}),$$

where

$$D(\mathbf{x}_i) \approx D_i = \frac{1}{\rho(\mathbf{x}_i)} \left(S_0 \psi_i^{(0),1} E_{\min} + \sum_{n=1}^{N-1} \frac{(S\psi^{(0)})_i^n + (S\psi^{(0)})_i^{n+1}}{2} (E^{n+1} - E^n) \right)$$

and $\psi_i^{(0),1} = (S\psi^{(0)})_i^1 / S_i(E_{\min})$.

4. Numerical examples

To assess the proposed limiting strategy in the context of dose calculation, we apply our realizability-preserving MCL scheme to representative test problems. For the energy discretization, we use Heun's method, a second-order explicit SSP-RK scheme. In view of condition (33), the time step ΔE is determined using the formula [24, 30, 31]

$$\Delta E = \frac{\text{CFL}}{\max_{i \in \{1, \dots, N_h\}} \frac{2}{m_i S_i} \sum_{j \in \mathcal{N}_i^*} d_{ij}},$$

where $\text{CFL} \leq 1$ is a given threshold. This choice of ΔE guarantees realizability, as shown in Sections 3.2 and 3.3.

The implementation of MCL used in our numerical experiments is based on the open-source C++ finite element library MFEM [2, 3, 40]. The two- and three-dimensional results are visualized in Paraview [5].

4.1. Analytical model

We begin by validating the proposed method against an analytical reference solution derived and verified with established Monte Carlo dose engines in [4]. Neglecting the scattering effects and assuming a perfectly collimated beam propagation in a single direction through a homogeneous medium reduces the Fokker–Planck equation (1) to a linear one-dimensional transport equation, which can be solved via

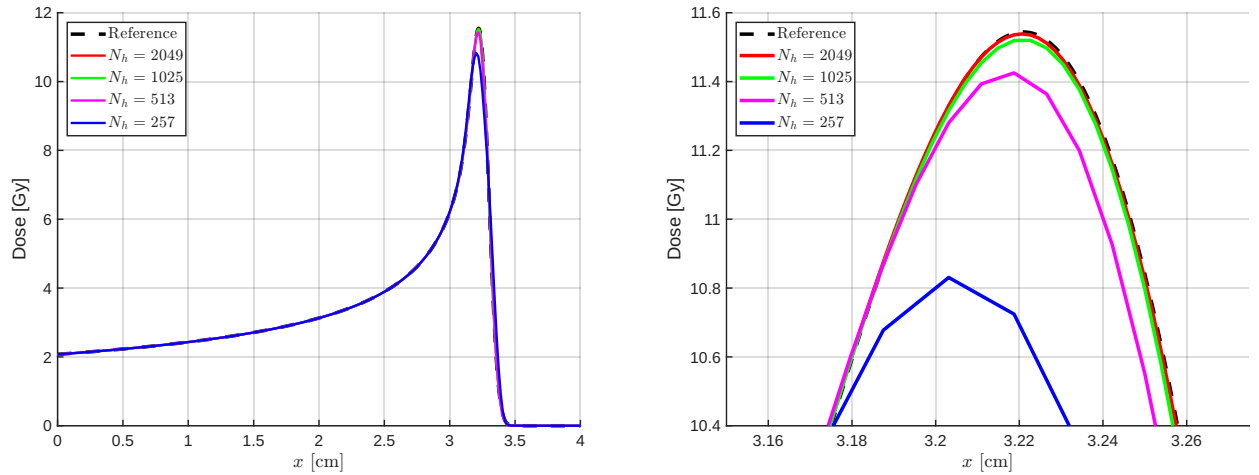
the method of characteristics. For a prescribed inflow fluence $g(E)$, the corresponding dose is obtained by integrating the analytical solution weighted by the stopping power (2), yielding [4]

$$D_{\text{ref}}(x) = \frac{1}{\beta p \rho(x)} \int_0^{E_{\text{max}}} \left(E^p + \frac{x}{\beta} \right)^{\frac{1-p}{p}} g \left(\left(E^p + \frac{x}{\beta} \right)^{\frac{1}{p}} \right) dE. \quad (51)$$

In this first test, we set the scattering power to $T = 0$ for a direct comparison with the analytical reference solution. Note that the scattering step (31) reduces to multiplication by unity. We consider a monoenergetic proton beam with energy $E_0 = 62 \text{ MeV}$ consisting of $\psi_0 = 1.21 \times 10^9$ protons in a water phantom. Thus, the material properties are $\rho = 1$, $\beta = 0.0022$, and $p = 1.77$ throughout the computational domain $\mathcal{D} = [0, 4] \text{ cm}$. The beam is prescribed at $x = 0$ using (47)–(48). Consistently, the inflow function used in the reference solution (51) is given by

$$g(E) = \psi_0 \frac{1}{\sqrt{2\pi} \sigma_E} \exp \left[-\frac{(E - E_0)^2}{2\sigma_E^2} \right].$$

In two further tests, we perform simulations in the three-dimensional domain $\mathcal{D} = [0, 4] \text{ cm} \times [0, 1.5] \text{ cm} \times [0, 1.5] \text{ cm}$. To assess the accuracy of the dose distributions computed with and without scattering, we compare them with the reference solution (51). For this comparison, the dose is integrated over the y - z plane perpendicular to the direction of beam propagation, as done in [4].



(a) One-dimensional dose distributions obtained on meshes of varying resolution.

(b) Close up of Bragg-peak region for the one-dimensional dose distributions.

Figure 1: One-dimensional dose distribution of a 62 MeV proton beam in a water phantom computed with the proposed MCL scheme on meshes with $N_h \in \{257, 513, 1025, 2049\}$ and CFL = 0.5. Scattering is neglected. Results are compared with the reference solution (51).

Figure 1 shows the one-dimensional dose distributions computed with the proposed MCL scheme for the M_1 model on a hierarchy of meshes. Away from the Bragg peak, even coarse meshes provide

accurate approximations of the dose profile, when compared to the reference solution (51). However, near the Bragg peak, coarse discretizations exhibit noticeable peak clipping. As the mesh is refined, the resolution of the peak improves significantly. On the finest mesh with $N_h = 2049$ nodes, the numerical solution agrees almost perfectly with the reference solution, despite employing the reduced M_1 moment model.

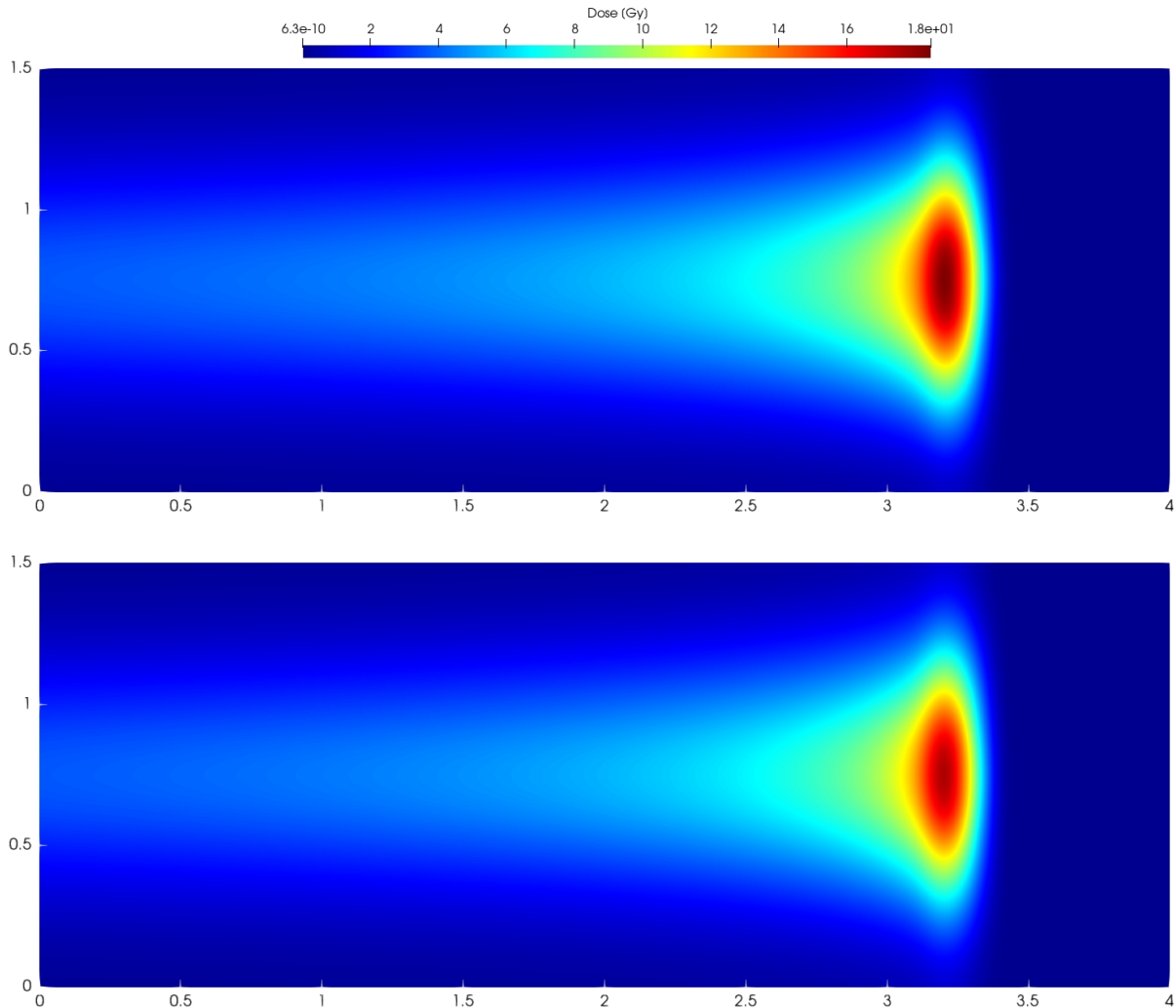
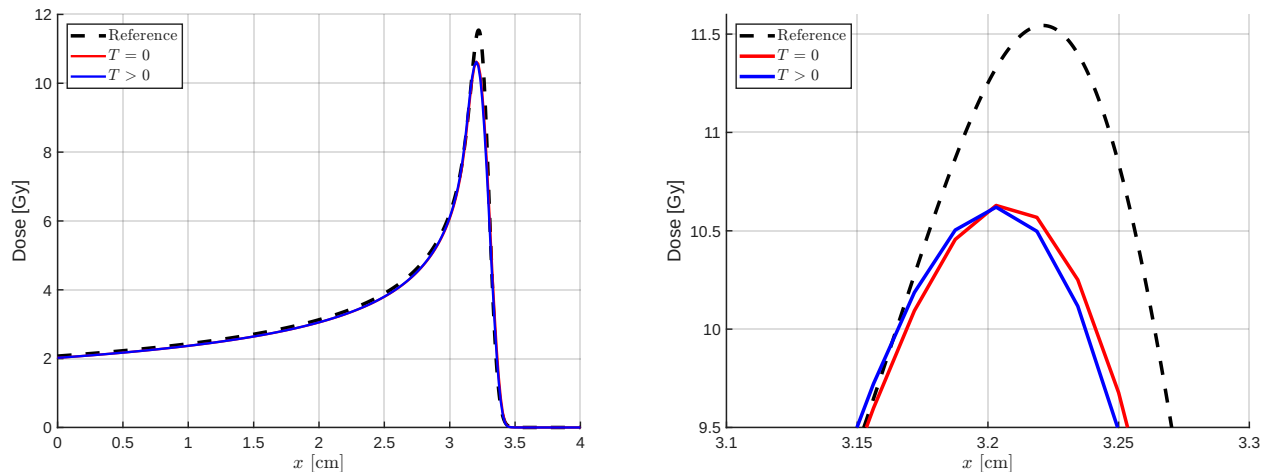


Figure 2: Three-dimensional dose distribution of a 62 MeV proton beam in a water phantom computed with the proposed realizability-preserving MCL scheme on a uniform hexahedral mesh with $N_h = 257 \times 97 \times 97$ nodes and CFL = 0.5. Shown are slices at $z = 0.75$ cm without scattering (top) and with scattering (bottom).

Slices of the three-dimensional solutions with and without scattering at $z = 0.75$ cm are shown in



(a) Three-dimensional dose distributions integrated over y - z planes.

(b) Close up of Bragg-peak region for the three-dimensional dose distributions integrated over y - z planes.

Figure 3: Three-dimensional dose distributions of a 62 MeV proton beam in a water phantom computed with the proposed MCL scheme on a mesh with $N_h = 257 \times 97 \times 97$ nodes and CFL = 0.5 with and without scattering effects. Results are integrated over y - z planes and compared with the reference solution (51).

Figure 2. Both simulations yield physically consistent dose distributions without any visible numerical artifacts. In the Bragg-peak region, the solution including scattering exhibits a slightly reduced peak.

The corresponding depth-dose curves obtained by integration over the y - z plane are shown in Figure 3. Both curves compare well with the reference solution. Minor peak clipping is observed, which can be attributed to the spatial resolution in the x -direction. The nearly identical peak magnitudes in the integrated curves indicate that the slight difference in peak dose observed in Figure 2 is due to lateral spreading of the dose profile caused by scattering.

4.2. 65 MeV beam in a patient

To illustrate the performance of the proposed limiting techniques in the presence of material discontinuities, we consider a three-dimensional simulation of a 65 MeV proton beam consisting of $\psi_0 = 1.21 \times 10^9$ protons propagating in the x -direction, prescribed at $x = 0$ using (47)–(48). The computational domain is $\mathcal{D} = [0, 4] \text{ cm} \times [0, 1.5] \text{ cm} \times [0, 1.5] \text{ cm}$, which is decomposed into four slabs of muscle, bone, lung, and water,

$$\begin{aligned}
 \mathcal{D}_{\text{muscle}} &= \{(x, y, z) \in \mathcal{D} : 0 \leq x < 1\}, \\
 \mathcal{D}_{\text{bone}} &= \{(x, y, z) \in \mathcal{D} : 1 \leq x < 1.25\}, \\
 \mathcal{D}_{\text{lung}} &= \{(x, y, z) \in \mathcal{D} : 1.25 \leq x < 3\}, \\
 \mathcal{D}_{\text{water}} &= \{(x, y, z) \in \mathcal{D} : 3 \leq x \leq 4\},
 \end{aligned}$$

respectively. The stopping and scattering powers are set constant in space within each material slab using the parameters given in Table 1.

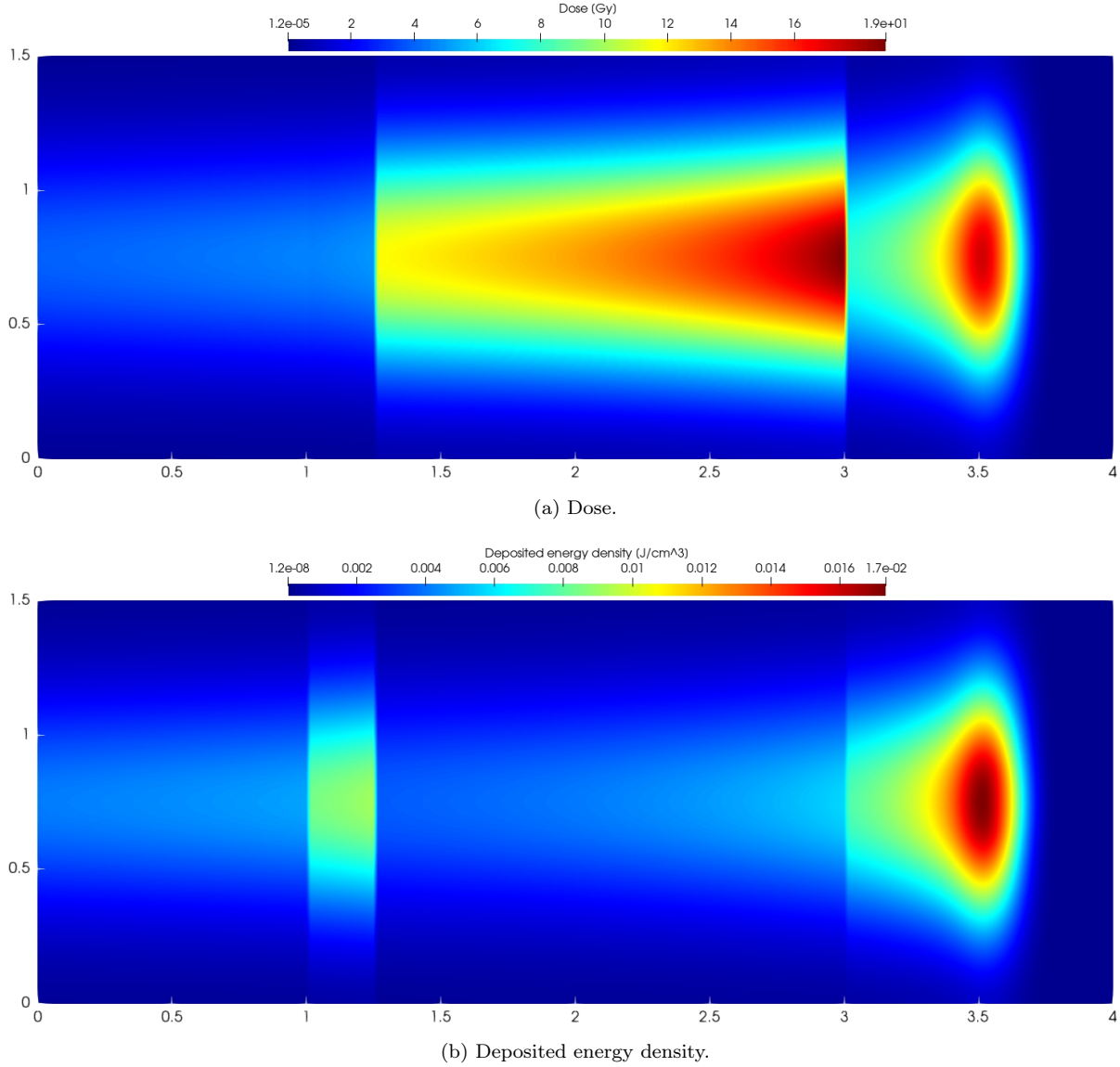


Figure 4: Three-dimensional dose distribution of a 65 MeV proton beam in a heterogeneous multi-material geometry computed with the proposed MCL scheme on a uniform hexahedral mesh with $N_h = 257 \times 97 \times 97$ nodes and CFL = 0.5. Shown are slices at $z = 0.75$ cm with dose (top) and deposited energy density (bottom).

Figure 4a shows a slice of the three-dimensional dose distribution at $z = 0.75$ cm. Since the interface between muscle and bone is not clearly visible in the dose distribution, we additionally visualize the

deposited energy density, ρD , in Figure 4b. All material interfaces are well resolved without any oscillations. No nonphysical states were detected during the simulation and no numerical artifacts are visible. This result demonstrates that the proposed realizability-preserving MCL scheme can resolve material discontinuities sharply while maintaining physical consistency.

4.3. Double beam problem

In the final numerical example, we illustrate a well-known drawback of the M_1 model. It turns out that the M_1 model cannot distinguish between two overlapping beams. This limitation arises because the zeroth and first angular moments of two intersecting beams coincide with those of a single beam propagating in the mean direction [49, Examples 2 and 3]. To illustrate this effect, we consider the two-dimensional computational domain $\mathcal{D} = [0, 4] \text{ cm} \times [0, 4] \text{ cm}$ consisting of water. Two proton beams with energy $E_0 = 62 \text{ MeV}$, each consisting of $\psi_0 = 1.21 \times 10^9$ protons, are prescribed at the midpoints of the left and lower boundaries, propagating in x - and y -directions, respectively.

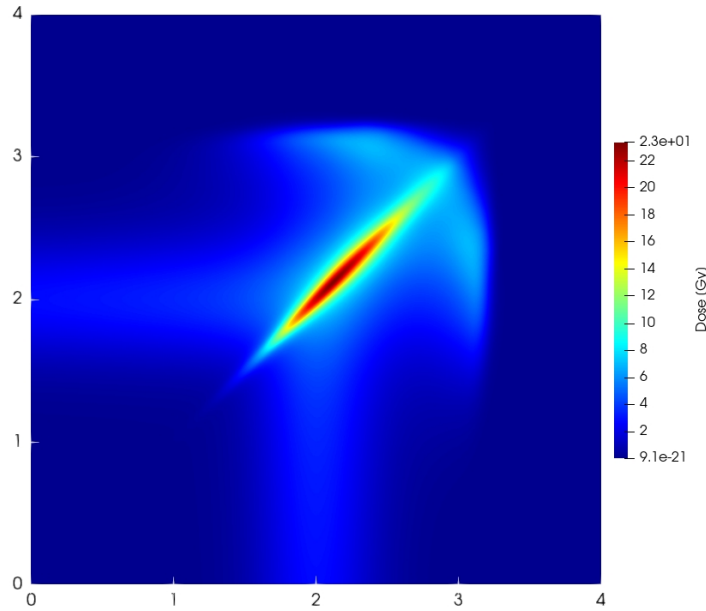


Figure 5: Dose distribution for two perpendicular proton beams in a water phantom computed with the proposed MCL scheme on a uniform rectangular mesh with $N_h = 257 \times 257$ nodes and $\text{CFL} = 0.5$.

As shown in Fig. 5, the beams intersect near the center of the computational domain and merge into a single beam traveling along the diagonal. This behavior is consistent with the literature and with [49, Examples 2 and 3]. Again, no nonphysical states were detected throughout the simulation and no numerical instabilities are visible in the numerical solution.

5. Conclusions

We have proposed a realizability-preserving MCL scheme for continuous finite element discretizations of the energy-dependent M_1 moment model of proton transport for dose calculation. Energy is treated as a pseudo-time variable, and a Strang splitting approach is employed to handle the scattering-induced forcing terms. The transport subproblem is discretized in energy using an explicit SSP-RK method. In this way, the moments are evolved backward in energy while preserving realizability at each substep. The dose is computed during the energy evolution using the trapezoidal rule to approximate the integral of the zeroth moment weighted by the stopping power.

Numerical experiments confirm that the proposed scheme produces stable and physically consistent dose distributions for both homogeneous media and heterogeneous material slabs in single-beam scenarios. The Bragg peak is well approximated when the mesh size is sufficiently small, and the scheme captures material interfaces in a sharp and well-resolved manner. However, the double-beam problem in Section 4.3 highlights a fundamental limitation of the M_1 moment model: overlapping beams merge into a single beam propagating in the mean direction.

This observation motivates the extension of the MCL methodology to continuous Galerkin discretizations of the M_2 moment model, in which the second moment $\psi^{(2)}$ is computed explicitly and the third moment is modeled by a closure relation [49]. In this setting, additional admissibility conditions arise in the form of eigenvalue constraints on the second-moment tensor. Limiting frameworks for tensor fields have been proposed in [30, 38, 39].

References

- [1] Graham W. Alldredge, Cory D. Hauck, and Andre L. Tits. High-order entropy-based closures for linear transport in slab geometry II: A computational study of the optimization problem. *SIAM J. Sci. Comput.*, 34(4):B361–B391, 2012.
- [2] Robert Anderson, Julian Andrej, Andrew Barker, Jamie Bramwell, Jean-Sylvain Camier, Jakub Cerveny, Veselin Dobrev, Yohann Dudouit, Aaron Fisher, Tzanio Kolev, Will Pazner, Mark Stowell, Vladimir Tomov, Ido Akkerman, Johann Dahm, David Medina, and Stefano Zampini. MFEM: A modular finite element methods library. *Comput. Math. Appl.*, 81:42–74, 2021.
- [3] Julian Andrej, Nabil Atallah, Jan-Phillip Bäcker, Jean-Sylvain Camier, Dylan Copeland, Veselin Dobrev, Yohann Dudouit, Tobias Duswald, Brendan Keith, Dohyun Kim, et al. High-performance finite elements with MFEM. *Int. J. High Perform. Comput. Appl.*, 38(5):447–467, 2024.
- [4] Ben S. Ashby, Veronika Chronholm, Daniel K. Hajnal, Alex Lukyanov, Katherine MacKenzie, Aaron Pim, and Tristan Pryer. Efficient proton transport modelling for proton beam therapy and biological quantification. *J. Math. Biol.*, 90(5), April 2025.
- [5] Utkarsh Ayachit. *The ParaView guide: A Parallel Visualization Application*. Kitware, Inc., 2015.
- [6] Gabriel R. Barrenechea and Petr Knobloch. Analysis of a group finite element formulation. *Appl. Numer. Math.*, 118:238–248, 2017.

- [7] James L. Bedford. Calculation of absorbed dose in radiotherapy by solution of the linear Boltzmann transport equations. *Phys. Med. Biol.*, 64(2):02TR01, 2019.
- [8] Martin J. Berger, J. S. Coursey, M. A. Zucker, and J. Chang. Stopping-powers and range tables for electrons, protons, and helium ions, NIST Standard Reference Database 124, 1993.
- [9] Christophe Berthon, Pierre Charrier, and Bruno Dubroca. An HLLC scheme to solve the M1 model of radiative transfer in two space dimensions. *J. Sci. Comput.*, 31:347–389, 2007.
- [10] Christophe Berthon, Martin Frank, Céline Sarazin, and Rodolphe Turpault. Numerical methods for balance laws with space dependent flux: Application to radiotherapy dose calculation. *Commun. Comput. Phys.*, 10(5):1184–1210, November 2011.
- [11] Thomas Bortfeld. An analytical approximation of the Bragg curve for therapeutic proton beams. *Med. Phys.*, 24(12):2024–2033, December 1997.
- [12] Thomas A. Brunner and James P. Holloway. Two new boundary conditions for use with the maximum entropy closure and an approximate Riemann solver. *Transport*, 10:3, 2000.
- [13] Thomas A. Brunner and James Paul Holloway. One-dimensional Riemann solvers and the maximum entropy closure. *J. Quant. Spectrosc. Radiat. Transfer*, 69(5):543–566, 2001.
- [14] Hans Burchard, Eric Deleersnijder, and Andreas Meister. A high-order conservative Patankar-type discretisation for stiff systems of production–destruction equations. *Appl. Numer. Math.*, 47(1):1–30, 2003.
- [15] Prince Chidyagwai, Martin Frank, Florian Schneider, and Benjamin Seibold. A comparative study of limiting strategies in discontinuous Galerkin schemes for the M_1 model of radiation transport. *J. Comput. Appl. Math.*, 342:399–418, 2018.
- [16] Jean-François Coulombel and Thierry Goudon. Entropy-based moment closure for kinetic equations: Riemann problem and invariant regions. *J. Hyperbol. Differ. Eq.*, 3(04):649–671, December 2006.
- [17] Alexander M. G. Cox, Laura Hattam, Andreas E. Kyprianou, and Tristan Pryer. A Bayesian inverse approach to proton therapy dose delivery verification. *Proceedings of the Royal Society A: Mathematical, Physical and Engineering Sciences*, 480(2301), November 2024.
- [18] Roland Duclous, Bruno Dubroca, and Martin Frank. A deterministic partial differential equation model for dose calculation in electron radiotherapy. *Phys. Med. Biol.*, 55(13):3843, 2010.
- [19] C.A.J. Fletcher. The group finite element formulation. *Computer Methods Appl. Mech. Engrg.*, 37(2):225–244, 1983.
- [20] Martin Frank, Cory D. Hauck, and Edgar Olbrant. Perturbed, entropy-based closure for radiative transfer. *arXiv preprint arXiv:1208.0772*, 2012.

- [21] Martin Frank, Hartmut Hensel, and Axel Klar. A fast and accurate moment method for the Fokker–Planck equation and applications to electron radiotherapy. *SIAM J. Appl. Math.*, 67(2):582–603, January 2007.
- [22] Kent A. Gifford, John L. Horton, Todd A. Wareing, Gregory Failla, and Firas Mourtada. Comparison of a finite-element multigroup discrete-ordinates code with Monte Carlo for radiotherapy calculations. *Phys. Med. Biol.*, 51(9):2253, 2006.
- [23] Bernard Gottschalk. On the scattering power of radiotherapy protons. *Medical Physics*, 37(1):352–367, December 2009.
- [24] Jean-Luc Guermond and Bojan Popov. Invariant domains and first-order continuous finite element approximation for hyperbolic systems. *SIAM J. Numer. Anal.*, 54(4):2466–2489, January 2016.
- [25] Hennes Hajduk. Monolithic convex limiting in discontinuous Galerkin discretizations of hyperbolic conservation laws. *Comput. Math. Appl.*, 87:120–138, April 2021.
- [26] Cory D. Hauck. High-order entropy-based closures for linear transport in slab geometry. *Commun. Math. Sci.*, 9(1):187–205, 2011.
- [27] Hartmut Hensel, Rodrigo Iza-Teran, and Norbert Siedow. Deterministic model for dose calculation in photon radiotherapy. *Phys. Med. Biol.*, 51(3):675–693, January 2006.
- [28] Martin Janson, Lars Glimelius, Albin Fredriksson, Erik Traneus, and Erik Engwall. Treatment planning of scanned proton beams in RayStation. *Med. Dosim.*, 49(1):2–12, 2024. Treatment Planning in Proton Therapy.
- [29] David S. Kershaw. Flux limiting nature’s own way – A new method for numerical solution of the transport equation. Technical report, Lawrence Livermore National Lab.(LLNL), Livermore, CA (United States), July 1976.
- [30] Dmitri Kuzmin. Monolithic convex limiting for continuous finite element discretizations of hyperbolic conservation laws. *Computer Methods Appl. Mech. Engrg.*, 361:112804, April 2020.
- [31] Dmitri Kuzmin and Hennes Hajduk. *Property-Preserving Numerical Schemes for Conservation Laws*. World Scientific, 2023.
- [32] Dmitri Kuzmin and Jari Hämäläinen. *Finite Element Methods for Computational Fluid Dynamics: A Practical Guide*. SIAM, 2014.
- [33] Dmitri Kuzmin, Matthias Möller, John N. Shadid, and Mikhail Shashkov. Failsafe flux limiting and constrained data projections for equations of gas dynamics. *J. Comput. Phys.*, 229(23):8766–8779, November 2010.
- [34] Edward W. Larsen, Moyed M. Miften, Benedick A. Fraass, and Iain A. D. Bruinvis. Electron dose calculations using the Method of Moments. *Med. Phys.*, 24(1):111–125, January 1997.

- [35] C. David Levermore. Relating Eddington factors to flux limiters. *J. Quant. Spectrosc. Radiat. Transfer*, 31(2):149–160, February 1984.
- [36] C. David Levermore. Moment closure hierarchies for kinetic theories. *J. Stat. Phys.*, 83(5–6):1021–1065, June 1996.
- [37] Liyong Lin, Paige A. Taylor, Jiajian Shen, Jatinder Saini, Minglei Kang, Charles B. Simone II, Jeffrey D. Bradley, Zuofeng Li, and Ying Xiao. NRG oncology survey of Monte Carlo dose calculation use in US proton therapy centers. *International Journal of Particle Therapy*, 8(2):73–81, 2021.
- [38] Christoph Lohmann. Flux-corrected transport algorithms preserving the eigenvalue range of symmetric tensor quantities. *J. Comput. Phys.*, 350:907–926, December 2017.
- [39] Christoph Lohmann. *Physics-Compatible Finite Element Methods for Scalar and Tensorial Advection Problems*. Springer Spektrum, 2019.
- [40] MFEM: Modular Finite Element Methods [Software]. <https://mfem.org>.
- [41] Gerald N. Minerbo. Maximum entropy Eddington factors. *J. Quant. Spectrosc. Radiat. Transfer*, 20(6):541–545, December 1978.
- [42] Philipp Monreal and Martin Frank. *Moment Realizability and Kershaw Closures in Radiative Transfer*. PhD thesis, RWTH Aachen University, 2013.
- [43] J. E. Morel. Fokker-Planck calculations using standard discrete ordinates transport codes. *Nucl. Sci. Eng.*, 79(4):340–356, December 1981.
- [44] Paul Moujaes and Dmitri Kuzmin. Monolithic convex limiting and implicit pseudo-time stepping for calculating steady-state solutions of the Euler equations. *J. Comput. Phys.*, 523:113687, 2025.
- [45] Paul Moujaes, Dmitri Kuzmin, and Christian Bäumer. Realizability-preserving monolithic convex limiting in continuous Galerkin discretizations of the M1 model of radiative transfer. *Math. Comput. Simulat.*, 246:570–590, August 2026.
- [46] Wayne D. Newhauser and Rui Zhang. The physics of proton therapy. *Phys. Med. Biol.*, 60(8):R155–R209, March 2015.
- [47] null IAEA. *Neutron Monitoring for Radiation Protection*. Number v.115 in Safety Reports Series No Series. International Atomic Energy Agency, Vienna, 1st ed. edition, 2024. Description based on publisher supplied metadata and other sources.
- [48] Edgar Olbrant, Cory D. Hauck, and Martin Frank. A realizability-preserving discontinuous Galerkin method for the M1 model of radiative transfer. *J. Comput. Phys.*, 231(17):5612–5639, 2012.

- [49] Teddy Pichard, Graham W. Alldredge, Stéphane Brull, Bruno Dubroca, and Martin Frank. An approximation of the M_2 closure: Application to radiotherapy dose simulation. *J. Sci. Comput.*, 71(1):71–108, 2017.
- [50] Teddy Pichard, Denise Aregba-Driollet, Stéphane Brull, Bruno Dubroca, and Martin Frank. Relaxation schemes for the M_1 model with space-dependent flux: Application to radiotherapy dose calculation. *Commun. Comput. Phys.*, 19(1):168–191, 2016.
- [51] Jatinder Saini, Erik Traneus, Dominic Maes, Rajesh Regmi, Stephen R. Bowen, Charles Bloch, and Tony Wong. Advanced proton beam dosimetry part I: Review and performance evaluation of dose calculation algorithms. *Translational Lung Cancer Research*, 7(2), 2018.
- [52] Pia Stammer, Niklas Wahl, Jonas Kusch, and Danny Lathouwers. A high-order deterministic dynamical low-rank method for proton transport in heterogeneous media, 2025.
- [53] S. B. Uilkema. Proton Therapy Planning using the SN Method with the Fokker-Planck Approximation. Master’s thesis, TU Delft, 2012.
- [54] W. Ulmer. Theoretical aspects of energy–range relations, stopping power and energy straggling of protons. *Radiat. Phys. Chem.*, 76(7):1089–1107, July 2007.
- [55] Oleg N. Vassiliev, Todd A. Wareing, John McGhee, Gregory Failla, Mohammad R. Salehpour, and Firas Mourtada. Validation of a new grid-based Boltzmann equation solver for dose calculation in radiotherapy with photon beams. *Phys. Med. Biol.*, 55(3):581, 2010.
- [56] Nico Verbeek, Jörg Wulff, Martin Janson, Christian Bäumer, Sameera Zahid, Beate Timmermann, and Lorenzo Brualla. Experiments and Monte Carlo simulations on multiple Coulomb scattering of protons. *Med. Phys.*, 48(6):3186–3199, May 2021.